Third order modal exceptional degeneracy in waveguides with glide-time symmetry

Farshad Yazdi ◉, Tarek Mealy ◉, Alireza Nikzamir ◉, Robert Marosi ◉, and Filippo Capolino ◉*

Department of Electrical Engineering and Computer Science, University of California, Irvine, California 92697, USA

The dispersion of a three-way waveguide is engineered to exhibit exceptional modal characteristics. Two coupled waveguides with *parity-time* ($\mathcal{PT}$) symmetry have been previously demonstrated to exhibit second order exceptional points of degeneracy (EPDs). In this work, we introduce and investigate a particular class of EPDs, applicable from radio frequency to optical wavelengths, whereby three coupled waveguides satisfy *glide-time* ($\mathcal{GT}$) symmetry to exhibit a third order modal degeneracy with a real-valued wave number. $\mathcal{GT}$ symmetry involves glide symmetry of lossless and gainless components of the waveguide in addition to changing the sign of passive and active elements while applying a glide-symmetry operation. This $\mathcal{GT}$-symmetry condition allows three Floquet-Bloch eigenmodes of the structure to coalesce to a real-valued wave number at a single frequency, in addition to having one branch of the dispersion diagram with a purely real wave number. The proposed scheme may have applications including but not limited to distributed amplifiers, radiating arrays, and sensors, from radio frequency to optics.

I. INTRODUCTION

We propose and investigate a periodic three-way electromagnetic waveguide with a *glide-time* ($\mathcal{GT}$)-symmetric topology that exhibits a distinguished class of degeneracy conditions based on the coalescence of three degenerate modes with a real wave number. The concept presented in this paper is based on applying concepts inspired by $\mathcal{PT}$ symmetry [1,2] to a glide-symmetric waveguide [3]. We call this combination $\mathcal{GT}$ symmetry. It is different from $\mathcal{PT}$ symmetry since the waveguide does not possess parity symmetry. In this paper we show that a waveguide with $\mathcal{GT}$ symmetry, i.e., with a balanced condition of gain and loss, possesses an exceptional point of degeneracy (EPD) of order 3, with a real-valued wave number.

Exceptional degeneracies of order 2, 3, and 4 of eigenmodes in periodic media have been previously investigated in [4–10], demonstrating the existence of unique features associated with modal degeneracies; even though they did not name them "exceptional points," they provided the math and physics associated with such degeneracy points. Exceptional points and their perturbation have been studied previously in more general terms [11–14] (note that the term "exceptional point" had already been mentioned in the 1966 book by Kato [13], Chap. 2). These degeneracies are not just in the eigenvalues but also in the polarization states (eigenvectors).

The concept of EPD associated with the coalescence of modes is relatively recent in the study of active devices. The recent interest in this class of degeneracies was mainly motivated by their relevance in the study of *parity-time* ($\mathcal{PT}$) -symmetric systems in physics [1,2,15–25].

The $\mathcal{GT}$-symmetric waveguide in this paper is implemented by adding balanced gain and loss (it can be radiation loss due to antennas radiation), to a glide-symmetric waveguide. A periodic waveguide is said to possess glide ($\mathcal{G}$) symmetry if it remains invariant under the glide operation, consisting of a translation by half of the geometrical period d, followed by a reflection in the so-called glide plane [3,26–33]. We define $\mathcal{GT}$ symmetry as regular glide symmetry of lossless and gainless components of the waveguide, in addition to changing the sign of passive and active elements while applying such glide-symmetry operation. In other words, it is a combination of $\mathcal{PT}$ symmetry and glide symmetry.

Previously, different kinds of EPDs have been found in lossless guiding structures in [4–6,20,34,35]. In particular, an EPD of order 3 in a lossless waveguide, called the stationary inflection point (SIP) has been demonstrated in [34,36–38], whereas an EPD of order 4 in lossless waveguides, referred to as the degenerate band edge (DBE), has been demonstrated in multimode waveguides [7,39–44].

A third order EPD occurs when three eigenmodes of the system coalesce in both their eigenvalues and eigenvectors. EPD conditions (i.e., where the eigenvectors degenerate) cannot be found when the associated matrix describing propagation in the system is Hermitian. However, as described previously in [4–7,9,38,41,42,45,46], the dynamics of the fields in a waveguide that does not have loss or gain may still be described using a non-Hermitian matrix, where such matrix becomes similar to one that contains a nontrivial Jordan block; this is the case for an SIP. A more precise description about Hermiticity is provided in [47].

To clarify, a third order EPD that occurs in lossless and gainless waveguides is often referred to as the stationary inflection point (SIP) or frozen mode regime. The SIP is obtained by the coalescence of three eigenmodes (in eigenvalues and eigenvectors), where two eigenmodes are evanescent and

---

one eigenmode is propagating to form a frozen mode that has a vanishing group velocity at a particular frequency. When the waveguide possesses gain and loss, the possibility to find a mode with a purely real wave number and a degeneracy of order 3 is not apparent; this paper shows that it is possible. We use the more general term "third order EPD" rather than "SIP" here to describe this third order eigenmode coalescence in the presence of gain and loss. Therefore, the SIP is a special case of a third order EPD. In other words, the SIP is a third order EPD, but not all third order EPDs are SIPs.

At radio frequency (rf), the SIP was experimentally demonstrated in a three-way waveguide made of three coupled microstrips in [38]. The occurrence of the DBE has also been experimentally demonstrated at rf in [41,42,47]. In [48], the authors experimentally demonstrated a split band edge, which is a degeneracy closely related to the DBE, in a metallic circular waveguide loaded with anisotropic scatterers.

On the other hand, EPDs of order 2, 3, and 4 have been demonstrated theoretically and experimentally in [2,49–55] and [17,47,56,57], respectively, by proper balancing of the loss and gain, using the concept of $\mathcal{PT}$ and anti-$\mathcal{PT}$ symmetry.

The general subject of this paper is the investigation of third order modal degeneracy in a three-way waveguide with balanced loss and gain, satisfying $\mathcal{GT}$ symmetry. For waveguides made of three coupled transmission lines (i.e., three ways) like the one we consider in this work, the allowed orders of EPD are second, third, fourth, and sixth. The third order EPD is the only one that does not have a stopband above or below the EPD frequency (it is the only odd order) and has a group velocity that does not change sign above and below the EPD frequency. This makes the third order EPD beneficial for amplifier applications. (For an amplifier application of an SIP, i.e., a third order EPD without gain and loss, see [58].)

In the vicinity of third order EPDs, the dispersion diagram of eigenmodes in a periodic waveguide satisfies $(\omega - \omega_e) \propto (k - k_e)^3$, where ω_e is the angular frequency at which three modes coalesce and k_e is the real-valued Bloch wave number at the degeneracy point. Note that $k_e \neq \pi/d$, meaning that the EPD will not occur at the edge, or middle, of the Brillouin zone. An illustration of an ideal dispersion relation exhibiting a third order EPD is shown in Fig. 1(a), where only the real branch of the $\omega-k$ dispersion diagram (where k is the Bloch-wave number and ω is the angular frequency) is shown. This kind of degeneracy obtained in a lossless waveguide has been named SIP. Here, instead, we investigate the occurrence of analogous third order EPDs in $\mathcal{GT}$-symmetric waveguides, i.e., where both gain and losses are present. The periodic set of losses in the $\mathcal{GT}$-symmetric waveguide in Fig. 1 represent the radiation resistances of an array of antennas.

The fundamental concept offered here is potentially useful for a variety of applications. Indeed, the use of the DBE has been proposed already for low threshold oscillators with a stable oscillation frequency [59–61]. Recently the DBE oscillator has been experimentally demonstrated in [62]. Oscillators based on EPD with balanced loss and gain have been proposed in [50,51,63,64] that are, in principle, able to radiate high power.

The SIP application has been proposed for delay lines [37]. High efficiency, high gain amplifiers based on SIP have also
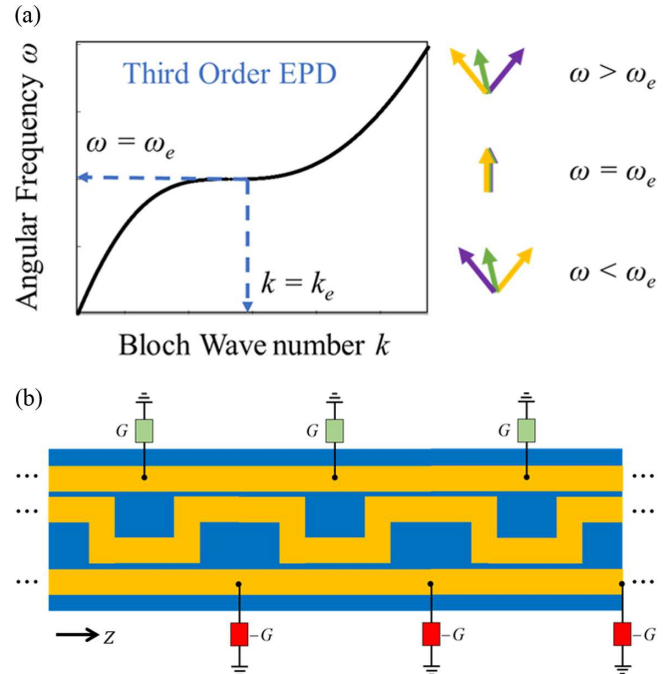

FIG. 1. (a) An example of dispersion relation of the mode with purely real wave number in an infinitely long periodic waveguide made of three coupled waveguides with loss and gain satisfying $\mathcal{GT}$ symmetry. The third order EPD occurs at the angular frequency ω_e with real-valued Floquet-Bloch wave number k_e, where three eigenvectors (schematically represented by three vectors) coalesce. (b) As an example, the three-way periodic waveguide with third order EPD is made of three coupled microstrips over a grounded substrate (in blue) with periodic gain and loss, shifted by half a period. The structure in (b) can be seen in a more general way as two transmission lines coupled through a third serpentine transmission line. The three-way periodic waveguide supports three modes in each longitudinal direction.

been proposed in [58] based on the concept of *three-mode synchronization*, in traveling wave tubes.

The third order EPD studied here can be applied to the case of distributed amplifiers interleaved with an array of antennas for high power radiation, since, in principle, the EPD can be designed with large gain balanced with large radiation loss.

The paper is organized as follows: in Sec. II, we introduce and discuss the two kinds of unit-cell structures for the three-way waveguide, where the transfer matrix of the unit cell is modeled using coupled transmission lines (CTLs). The modal dispersion of the periodic structure is investigated where we demonstrate the existence of third order EPDs in the dispersion diagram for a few designs. We also provide a thorough analysis of the power distribution for the semi-infinite structure as well as the engineering of the dispersion diagram to have different characteristics by tuning the parameters of the unit cell. Section III is dedicated to the finite length studies of the periodic structure with proper terminations where we study the resonance behavior and stability through the S parameters of the three-way waveguide. We also investigate the power performance of the finite-length structure for a distributed radiating amplifier application and its important characteristic aspects such as stability analysis and radiating
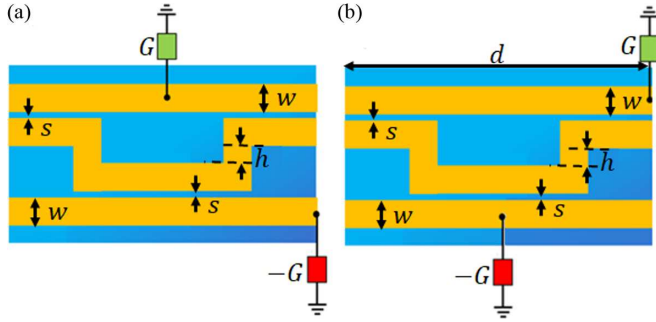
FIG. 2. (a) Unit cell of the three-way periodic microstrip structure that exhibits a third order degeneracy for case A (also used in Secs. III and IV). The structure is composed of two uniform transmission lines coupled through a third serpentine transmission line in the middle, and two shunt conductances, gain and passive (e.g., a radiation resistance), added to the uncoupled sections with real positive and negative values as shown. (b) Unit cell of an alternative design (case B and case C) of the three-way periodic microstrip structure where the shunt conductances (gain and loss) are added to the coupled sections instead.

and load power gains. Throughout this paper, we implicitly assume that the time dependence is in the form of $e^{j\omega t}$.

II. THREE-WAY COUPLED WAVEGUIDE WITH $\mathcal{GT}$ SYMMETRY

We define $\mathcal{GT}$ symmetry as the combination of two operators: the $\mathcal{G}$ glide symmetry, and the $\mathcal{T}$ time reversal symmetry operators. In the modeling of an electromagnetic system, the time reversal operators $\mathcal{T}$ makes the imaginary unit $j \to -j$, hence when applied to a refractive index, it implies that $n(x,z) \to n^*(x,z)$, i.e., loss goes into gain and vice versa. The glide-symmetry operators $\mathcal{G}$ makes a translation by half of the geometrical period d, followed by a reflection in x. In terms of refractive index, it implies that $n(x,z) \to n(-x, z + d/2)$, The glide symmetry is considered a higher symmetry. The combined $\mathcal{GT}$ operator leads to $n(x,z) \to n^*(-x, z + d/2)$.

In the following we investigate a three-way waveguide that satisfies these properties. However, we focus on a metal-dielectric structure with lumped loss and gain, which is described in more detail in the next section.

The goal of this paper is to show that a structure that satisfies $\mathcal{GT}$ symmetry has a third order EPD with a real-valued wave number. The study of the spectrum of the $\mathcal{GT}$ operator is left to future investigations.

A. Unit-cell design of the coupled serpentine waveguide with gain and loss

We consider two distinct periodic waveguide geometries in microstrip technology based on the three-way CTLs with unit cells as shown in Fig. 2. The designs are modeled by two uniform transmission lines that are coupled through a third serpentine-shaped transmission line in the middle, similar to the structure in [38]. In this paper, we have altered the structure by adding balanced gain and loss. This is implemented using a set of periodic lumped line-to-ground admittances on the first (top) microstrip with a conductance of $-G$ (gain) and

another set of periodic lumped line-to-ground admittances in the third (bottom) microstrip with the conductance of $+G$ (loss, or radiation loss) to achieve a $\mathcal{GT}$-symmetric design for the three-way microstrip structure. We find the degeneracy condition of order 3 by selecting proper periodic loss and gain values. The third order EPD is more general than the SIP that is found in passive, lossless three-way waveguides. However, the presence of lumped gain and loss elements makes the system more complicated. In terms of applications, the periodic gain provides amplification and losses may represent discrete radiating elements (e.g., antennas). Therefore, this scheme can be viewed either as a distributed radiating amplifier or as a structure that may radiate and oscillate (i.e., lasing) at the same time. Moreover, the degeneracy may bring advantages in terms of low noise, enhanced coherency among the radiating elements, etc.

We provide two potential implementations of such a $\mathcal{GT}$-symmetric structure: In Fig. 2(a), the discrete gain and loss elements are located at the uncoupled sections of the CTLs whereas in Fig. 2(b) they are located at the coupled sections. We provide in Appendix A the design parameters for both structures in Fig. 2. We assume that the conductance G has a pure real value representing either loss or gain in the structure. The three-way CTL supports three modes in each longitudinal direction. Thus, the structure can exhibit a third order EPD by tuning the microstrip geometry and admittances. In designing the unit cell to attain the EPD, for the sake of simplicity, it is assumed that all the transmission lines have the same width w, same separation distance between the coupled lines s, and the length of each unit cell is set to d. We used a substrate with a relative dielectric constant of 2.2, no loss tangent [$\tan(\delta) = 0$], and height of $h_s = 1.575$ mm. Also, the microstrip and ground plane metal layers were assumed to be lossless. To achieve the degeneracy condition at the desired frequency ($f_e = 2$ GHz), we fixed values for some of the dimensions including $w = 5$ mm for the linewidths (corresponding to lines with $Z_0 = 50\,\Omega$ characteristic impedance, when uncoupled) and $s = 0.5$ mm for the distance between the lines. We then tune other dimensions such as the length of the unit cell d, the height of the serpentine section h, and the value of the conductance G, to search for the third order degeneracy at the desired frequency. The optimization we have done to find a third order EPD is based on tuning the prementioned parameters to minimize the coalescence parameter associated with three eigenmodes in the system, as will be discussed later.

B. Transfer matrix formalism

We use a three-CTL transfer matrix formalism to construct the total transfer matrix for a single unit cell, in analogy to what was done in [38,47,51]. We will also use this transfer matrix in our analysis of the finite-length periodic structure composed of cascaded unit cells to model and investigate the various aspects of the modal degeneracy under study. The details of the transfer matrix formalism are provided in Appendix B. Other related matrix-based approaches have previously been used to analyze systems under $\mathcal{PT}$- and broken $\mathcal{PT}$-symmetry regimes in works such as [51,65–69].

In the investigation of the EPDs' properties through transfer matrix and eigenvalues for a six-port system, it is

convenient to define the position-dependent state vector in the form

$$\mathbf{\Psi}(z) = [V_1, \ Z_0 I_1, \ V_2, \ Z_0 I_2, \ V_3, \ Z_0 I_3]^{\mathrm{T}}, \qquad (1)$$

where voltages and currents are evaluated at z along the three-way CTLs. The state vector describes the spatial evolution of the eigenmodes as they propagate through the structure. A *transfer matrix*, $\underline{\mathbf{T}}(z_2, z_1)$, is used, which uniquely relates the state vector $\mathbf{\Psi}(z)$ between two points in the structure such that

$$\mathbf{\Psi}(z_2) = \underline{\mathbf{T}}(z_2, z_1)\mathbf{\Psi}(z_1), \qquad (2)$$

where we use the forward transfer matrix notation with $z_2 > z_1$ along the z axis. The 6×6 transfer matrix $\mathbf{T}_U$ of a unit cell shown in Fig. 2(a) is then defined as $\mathbf{\Psi}(z + d) = \mathbf{T}_U \mathbf{\Psi}(z)$ and is expressed and calculated in terms of the geometric and electrical parameters of the unit cell using formulas found in Appendix B. Accordingly, the unit-cell transfer matrix for the waveguide in Fig. 2(a) is obtained by cascading the transfer matrices of each segment of the unit cell:

$$\mathbf{T}_U = \underline{\mathbf{T}}_{-G}\underline{\mathbf{T}}_A\underline{\mathbf{T}}_C\underline{\mathbf{T}}_B\underline{\mathbf{T}}_{+G}\underline{\mathbf{T}}_B\underline{\mathbf{T}}_C\underline{\mathbf{T}}_A. \qquad (3)$$

The expression for the unit-cell transfer matrix for Fig. 2(b) is presented in Appendix B. For an infinitely long stack of CTL unit cells, a pseudoperiodic solution for the state vector $\mathbf{\Psi}(z)$ exists in the Bloch form and the transfer matrix $\mathbf{T}_U$ translates the state vector across a unit cell as the eigenvalue equation of

$$\mathbf{T}_U \ \mathbf{\Psi}(z) = e^{-jkd}\mathbf{\Psi}(z), \qquad (4)$$

where k is the complex-valued Bloch wave number. The eigenvalues of the transfer matrix and hence the Bloch wave number are obtained as solutions of the characteristic equation,

$$\mathrm{Det}(\mathbf{T}_U - \zeta\underline{\mathbf{I}}) = 0, \qquad (5)$$

in which we define $\underline{\mathbf{I}}$ to be the 6×6 identity matrix. For the CTL with three lines (6×6 transfer matrix) discussed in this study, six eigenvalues, $\zeta_i = e^{-jk_i d}$, with $i = 1, 2, \ldots, 6$, of the $\mathbf{T}_U$ matrix are calculated from Eq. (5).

Note that, because of periodicity, each eigenvalue corresponds to an infinite set of wave numbers $k_i + n2\pi/d$, with $n = 0, \pm1, \pm2, \ldots$, called Floquet harmonics. In the following, we show the dispersion diagrams with wave numbers in the range $0 < \mathrm{Re}(k) < 2\pi/d$ that we refer to as the fundamental Brillouin zone.

Because of the reciprocity of the system, the transfer matrix satisfies $\mathrm{Det}(\mathbf{T}_U) = 1$. Consequently, if ζ is an eigenvalue of the system then ζ^{-1} is another eigenvalue. Therefore, the modes supported by the structure have wave numbers $k_1, k_2, k_3, -k_1, -k_2$, and $-k_3$. At the third order EPD studied in this paper, three eigenvalues coalesce at k_e while the other three coalesce at $-k_e$. Moreover, at the EPD, the transfer matrix $\mathbf{T}_U$ cannot be diagonalized because the three eigenvectors of (4) associated with each k_e and $-k_e$ wave number coalesce, as discussed in [38,43]. The coalescence of three eigenvectors is a necessary and sufficient condition for a third order EPD to occur. This means that the existence of an EPD can be found by checking the coalescence of three eigenvectors. This is the technique implemented in this paper to find the EPD

conditions while maintaining $\mathcal{G}\mathcal{T}$ symmetry. At the EPD, only two polarizations states, $\mathbf{\Psi}_{e1}$ and $\mathbf{\Psi}_{e2}$, are the eigenvectors of the system. This implies that the geometric multiplicity of each degenerate eigenvalue is equal to 1 while its algebraic multiplicity is equal to 3; hence the transfer matrix $\mathbf{T}_U$ is not diagonalizable and it is similar to a matrix containing two Jordan blocks of dimensions 3×3, as explained in detail in [43]. At the EPD, the transfer matrix $\mathbf{T}_U$ is represented as

$$\mathbf{T}_U = \underline{\mathbf{V}}\begin{bmatrix} \underline{\underline{\mathbf{\Lambda}}}_{\mathrm{J},1} & \underline{\underline{\mathbf{0}}} \\ \underline{\underline{\mathbf{0}}} & \underline{\underline{\mathbf{\Lambda}}}_{\mathrm{J},2} \end{bmatrix}\underline{\mathbf{V}}^{-1}, \qquad (6)$$

where $\underline{\underline{\mathbf{\Lambda}}}_{\mathrm{J},1}$ and $\underline{\underline{\mathbf{\Lambda}}}_{\mathrm{J},2}$ are two Jordan blocks,

$$\underline{\underline{\mathbf{\Lambda}}}_{\mathrm{J},1} = \begin{bmatrix} \zeta_e & 1 & 0 \\ 0 & \zeta_e & 1 \\ 0 & 0 & \zeta_e \end{bmatrix}, \quad \underline{\underline{\mathbf{\Lambda}}}_{\mathrm{J},2} = \begin{bmatrix} \zeta_e^{-1} & 1 & 0 \\ 0 & \zeta_e^{-1} & 1 \\ 0 & 0 & \zeta_e^{-1} \end{bmatrix}, \tag{7}$$

and the similarity transformation matrix $\underline{\mathbf{V}}$ is composed of one degenerate eigenvector and two generalized eigenvectors, associated with each of the eigenvalues ζ_e and ζ_e^{-1}.

The theory explained in [43] is for a lossless three-way waveguide but there are many similarities with the waveguide in this paper which has periodic gain and loss elements. Also in this paper, we find a branch of the dispersion diagram that corresponds to a purely real wave number (shown in Fig. 1), while the other two branches in Figs. 3–5 represent waves with complex wave numbers, as discussed in the next section.

C. Dispersion relation and coalescence parameter featuring third order EPD

The periodic three-way microstrip in Fig. 2 can support a third order degeneracy. We design three different CTLs (cases A, B, and C) where the EPD occurs at an operating frequency of 2 GHz. Our unit-cell designs have been determined by using the fixed parameters provided in Appendix A, such as the microstrip width, spacing between coupled microstrips, substrate dielectric properties, and substrate thickness. We then tuned the other parameters such as the length of the unit cell d, the "height" h of the serpentine sections, and the choice of lumped gain and loss conductances $-G$ and G, respectively, to obtain EPDs at a desired frequency. Both the EPD frequency and the flatness of the dispersion curve in the vicinity of the degeneracy condition can be altered by tuning the dimensional and electrical parameters of the unit cell.

An EPD is represented by the coalescence of the eigenvalues (i.e., wave numbers) and by the coalescence of the eigenvectors (i.e., polarization states). The coalescence of the eigenvalues is necessary to have an EPD; however, the coalescence of the eigenvector guarantees the existence of an EPD. In the following, we assess the occurrence of a third order EPD by observing the coalescence of three eigenvectors. Accordingly, we define a figure of merit to measure how close the system is to an ideal third order degeneracy condition at the frequency of interest, called the *coalescence parameter* (C_{EPD}). This concept was developed in [47] for a fourth order degeneracy, and used also in [38] for an SIP; it is here
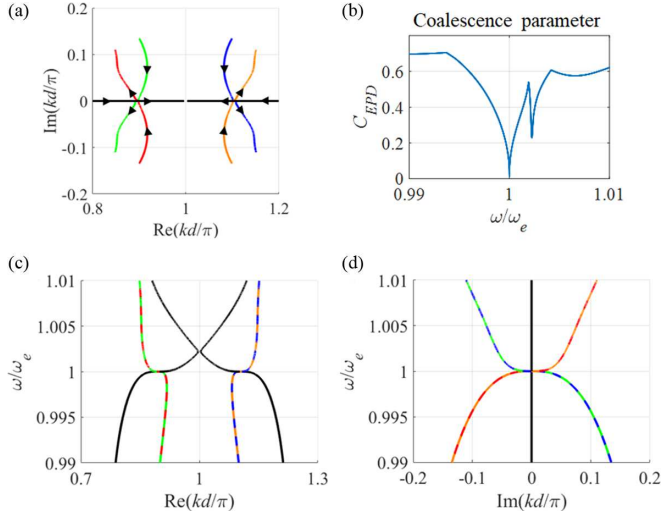
FIG. 3. Case A: (a) complex wave numbers plotted in the complex k plane varying frequency. This plot shows the existence of the third order modal degeneracy condition and coalescence of the three modes at two different EPD real-valued wave numbers, k_e and $-k_e + 2\pi/d$. It also shows than one branch is purely real. (b) Coalescence parameter plotted versus normalized frequency in the vicinity of the EPD. (c), (d) Typical modal dispersion diagram of the eigenmodes, showing both the real and imaginary parts of the normalized complex Floquet-Bloch wave number k versus normalized angular frequency around the EPD frequency ω_e. The purely real branches are shown in solid black. Dashed-line branches represent the modes with complex wave number and correspond to the complex branches of (a). The arrows along each branch of (a) indicate how the real and imaginary components of wave number vary as frequency is increased. Besides the lumped elements, we have assumed the three-way waveguide to be lossless for all the graphs shown in this figure.

analogously defined for a third order EPD as

$$C_{\text{EPD}} = \frac{1}{3} \sum_{\substack{m=1, n=2 \\ n>m}}^{3} |\sin(\theta_{mn})|, \quad \cos(\theta_{mn}) = \frac{\text{Re}|(\boldsymbol{\Psi}_m, \boldsymbol{\Psi}_n)|}{\|\boldsymbol{\Psi}_m\| \|\boldsymbol{\Psi}_n\|},$$

(8)

where θ_{mn} represents the angle between two eigenvectors $\boldsymbol{\Psi}_m$ and $\boldsymbol{\Psi}_n$ in a six-dimensional complex vector space, with norms $\|\boldsymbol{\Psi}_m\|$ and $\|\boldsymbol{\Psi}_n\|$, and $(\boldsymbol{\Psi}_m, \boldsymbol{\Psi}_n)$ is their inner product. The coalescence parameter defined in Eq. (8) is always positive, with small values indicating how well the eigenvectors of the structure are close to each other in the frequency range of interest. EPDs of third order occur when $C_{\text{EPD}} = 0$. Using this coalescence parameter as the error function to be minimized at the EPD frequency of interest, an optimization algorithm in MATLAB was used to select the conductance of the lumped elements, serpentine height h, and period of our unit cell d to make the device exhibit an EPD of third order.

We provide three examples of EPDs that occur in three-way microstrip waveguides as in Fig. 2, denoted as cases A, B and C. These cases were each found using the optimization method discussed above.

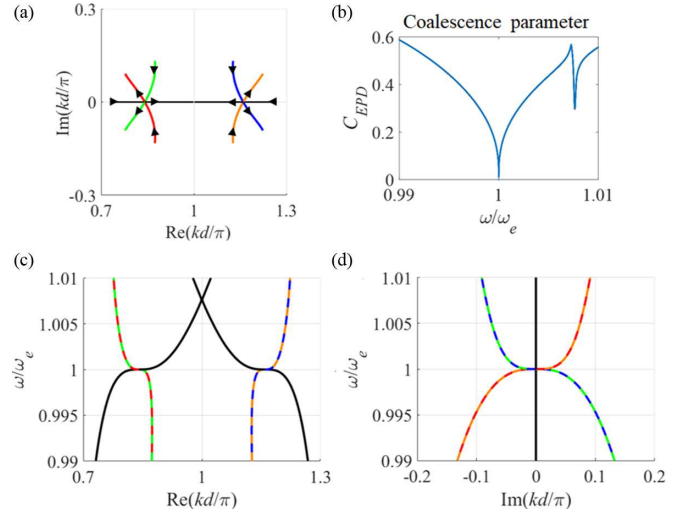Case A: In this example, the tuned unit-cell parameters were found to have a conductance value of $G = 0.1398$ S

(or equivalently $R = 1/G = 7.15\,\Omega$), serpentine height of $h = 5.35$ mm, and period of $d = 54.15$ mm. The active (gain) and passive conductances in this case are located on the unit cell as illustrated in Fig. 2(a).

Figure 3 shows the existence of third order degeneracy in the dispersion diagram and the coalescence parameter. The imaginary part of the dispersion diagram is plotted versus the real part in Fig. 3(a) where it shows the existence of the third order degeneracy condition and the coalescence of the three modes at two different locations in the fundamental Brillouin zone, at k_e and $-k_e + 2\pi/d$ due to reciprocity. In other words, we show an EPD in the region $0 < kd < \pi$, in the dispersion diagram of Fig 3(c). There are three coalescing branches, one (in solid black) has a purely real wave number with positive group velocity for frequencies around the EPD frequency, as can be seen by the black curve on the left side of Fig. 3(c). The second EPD is in the region $\pi < -kd + 2\pi < 2\pi$, where
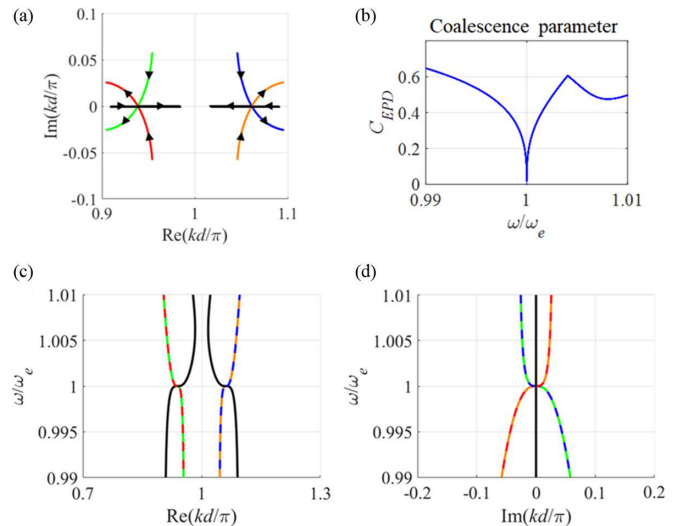

FIG. 4. Case B: The description is as in Fig. 3 but plots are for case B.

FIG. 5. Case C: The description is as in Fig. 3 but plots are for case C.

there are three coalescing branches. One branch (solid black) has a purely real wave number with negative group velocities for frequencies around the EPD. Through the rest of the paper, we consider the mode in the region $0 < k_e d < \pi$ as our EPD of interest associated with forward waves in our dispersion diagram.

In Fig 3(b), the coalescence parameter is plotted versus normalized frequency around ω_e (corresponds to 2 GHz) to demonstrate how close we are to the third order degeneracy condition in our design. Finally, in Figs. 3(c) and 3(d), we plot the modal dispersion diagram of the infinite structure, showing both the real and imaginary parts of the normalized complex Floquet-Bloch wave number k versus normalized angular frequency around the designed frequency ω_e where the third order behavior is observed. We used dashed lines in Figs. 3(c) and 3(d) for wave numbers that are complex valued to show different overlapping curves of real and imaginary parts. In other words, the curves with dashed lines of different colors represent two overlapping branches. We follow the same scheme in Figs. 4 and 5.

The normalized dispersion relation around the desired third order EPD can be approximated using the third order equation

$$(\omega/\omega_e - 1) \approx \zeta (kd/\pi - k_e d/\pi)^3, \tag{9}$$

where ω_e is the angular frequency at which three modes coalesce and k_e is the Floquet-Bloch wave number at the degeneracy point. The nondimensional parameter ζ determines the flatness of the normalized dispersion at the EPD which is related to the third derivative of $d^3\omega/dk^3$ around the degeneracy point. Lower values of the flatness factor ζ mean flatter dispersion relations at the EPD which is an important factor in designing a third order EPD for possible applications based on the desired characteristics and properties. For case A shown in Fig. 3 the flatness factor is calculated as $\zeta_A \approx 2.1$.

Case B: Using the same optimization method, we find additional solutions which exhibit third order modal degeneracy. The unit-cell design of case B differs from that of case A in that the lumped elements are positioned in the center of the coupled sections of the transmission line, as is illustrated in Fig. 2(b). For this second solution, the tuned unit cell was found to have the conductance value of $G = 0.105$ S (or equivalently $R = 1/G = 9.5\,\Omega$), serpentine height of $h = 6.36$ mm, and period of $d = 46.3$ mm. Like the previous case, the dispersion diagrams and coalescence parameter are plotted in Fig. 4, where we show the existence of the EPD for the new values and discuss its modal behavior. For the case B shown in Fig. 4, the flatness factor is calculated as $\zeta_B \approx 7.2$ which is higher than case A, meaning a narrower dispersion diagram compared to the previous case (i.e., less flat).

Case C: To show the flexibility of our design we have provided a third solution that exhibits third order modal degeneracy in its dispersion diagram by again tuning the dimensions around initial values which seem appropriate for a practical design and search for a new set of parameters to achieve the third order EPD. The tuned unit-cell parameters were found to be a conductance value of $G = 0.0099$ S (or equivalently $R = 1/G = 100.55\,\Omega$), serpentine height of $h = 1.07$ mm, and period of $d = 48.08$ mm. As in case B, the lumped elements are centered in the CTL sections, as illustrated in Fig. 2(b). The existence of the third order EPD
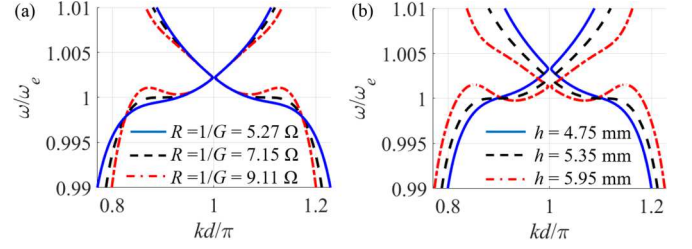

FIG. 6. Engineering of the dispersion diagram of the mode with purely real k to exhibit different group velocities (different slopes) around the EPD frequency. (a) By tuning the value of the R (or G) elements for case A we observe a slightly positive slope for $R = 5.27\,\Omega$ and a slightly negative slope for $R = 9.11\,\Omega$, whereas the ideal case with zero slope has $R = 7.15\,\Omega$. (b) By tuning the value of the h (serpentine height) for case A we observe a slightly positive slope for $h = 4.748$ mm and a slightly negative slope for $h = 5.948$ mm, whereas the ideal case with zero slope has $h = 5.948$ mm. For all the graphs shown above only the purely real branches of the dispersion diagram are plotted and we have assumed the structure to be lossless.

for this case is shown in the results of Fig. 5, where we have plotted the dispersion diagram and the coalescence parameter in a fashion similar to the previous cases. For case C shown in Fig. 5, the flatness factor is calculated as $\zeta_C \approx 188$ which is much higher than the two previous cases A and B indicating a more-narrow EPD in the dispersion diagram, as can be seen from the results in Fig. 5.

These three different solutions show that our design to achieve the third order modal degeneracy in the three-way CTL is flexible, and the parameters of interest can be tuned around some initial practical values based on the application.

D. Engineering of the dispersion diagram

One of the interesting features of the designs that we propose, which exhibit a third order modal degeneracy around a desired frequency, is that the slope of the dispersion diagram can be tuned easily by altering one or more design parameters of the unit cell. As a result, we can have a slightly positive local slope (small positive group velocity) or a slightly negative local slope (small negative group velocity) in proximity of the EPD, rather than the ideal case of zero slope. In Fig. 6(a), we show how the slope of the dispersion diagram for case A can be engineered to be positive or negative in the vicinity of the EPD by simply adjusting the value of $R = 1/G$, for both the gain and radiation loss elements while still maintaining $\mathcal{GT}$ symmetry in the system. We observe a slightly positive slope for slightly lower values of R ($R = 5.27\,\Omega$) than the EPD one of $R = 7.15\,\Omega$, shown in solid blue. We observe a slightly negative slope for $R = 9.11\,\Omega$, i.e., slightly higher than the EPD one, shown in dash-dotted red. The case with $R = 7.15\,\Omega$ that leads to the ideal third order EPD for case A with zero slope is shown in dashed black in Fig. 6(a). In this figure, we only show the branches with a purely real wave number; i.e., those with complex-valued k are not shown for simplicity.

Another method to alter the slope of the dispersion diagram in the vicinity of the third order degeneracy is by tuning the height of the serpentine microstrip (h) as shown in

Fig. 6(b). Note that by just altering h, the structure remains $\mathcal{GT}$ symmetric. As observed from the results of Fig. 6(b), by slightly lowering the height ($h = 4.75\,\mathrm{mm}$) we achieve slightly positive slope (shown in solid blue) compared to the dispersion diagram of case A, where the ideal EPD with zero slope occurs for $h = 5.35\,\mathrm{mm}$ (dashed black). Instead, by slightly increasing the height ($h = 5.95\,\mathrm{mm}$), we can also achieve a slightly negative slope (shown in dash-dotted red).

The results of these dispersion engineering examples demonstrate the flexibility of the proposed design for specific applications where the group velocity can be tuned by varying the design parameters about their nominal values. Increasing the slope of the dispersion diagram around the EPD frequency to reach a positive group velocity will potentially increase the bandwidth of the resonance peak associated with an EPD, which will be desirable for reaching higher bandwidth-gain products in amplifier applications [58]. Alternatively, decreasing the slope to negative values in the dispersion diagram around EPD results in higher Q factors for the EPD resonance peak [58], which may be beneficial for oscillator applications.

E. Power analysis based on modes around EPD

Exactly at the EPD ($\omega = \omega_e$), where three modes coalesce in their wave number $k_1 = k_2 = k_3 = k_e$, with k_e purely real [$\mathrm{Im}(k_e) = 0$], the eigenwaves propagating from unit cell to unit cell do not exhibit exponentially growing or decaying behavior. We checked this by using the single degenerate eigenvector as input state vector in a semi-infinite structure, i.e., $\boldsymbol{\Psi}(z = 0) = \boldsymbol{\Psi}_e$. This investigation of the power flow in the semi-infinite long periodic structure shows that at the EPD the power over G and $-G$ is balanced, meaning they both have equal powers that cancel one another (i.e., $P_{-G} = -P_G$), as is discussed later in this section.

The obtained dispersion diagrams, shown in Figs. 3–5, for the proposed $\mathcal{GT}$-symmetric structures show that, at frequencies slightly lower or higher than the EPD frequency, the three modes are slightly perturbed from the EPD, and they are no longer coalescing. These three modes have one mode that has a purely real wave number (black curves in Figs. 3–5), k_1, and the other two modes have wave numbers that are complex conjugates of each other (red and green curves in Figs. 3–5), $k_2 = k_3^*$. Another set of simulations was performed for the same proposed structures but with asymmetric gain and loss (broken $\mathcal{GT}$ symmetry) and we found that the dispersion diagram did not exhibit the prementioned conjugate property for the wave numbers $k_2 = k_3^*$.

Based on the prementioned conjugate property of the wave numbers, the proposed $\mathcal{GT}$-symmetric structures have two modal complex wave numbers with $\mathrm{Im}(k_2) = -\mathrm{Im}(k_3)$ which means that one mode is growing whereas the other one is the decaying mode along z. One (red curve) of those two modal complex wave numbers has $\mathrm{Im}(k_2) < 0$ for $\omega < \omega_e$ whereas it has $\mathrm{Im}(k_2) > 0$ for $\omega > \omega_e$. For the purely real mode k_1, there is no growing or decaying behavior in the signal and the power is balanced.

The mode with $\mathrm{Im}(k) > 0$ has a growing behavior in the signal over the unit cells moving along z. For this case, there is

more power provided by $-G$ (gain) than the power consumed by $+G$ (loss). Thus, the total power carried by this mode exiting a unit cell to the right is higher than the power entering the unit cell from the left. On the other hand, the mode with a negative imaginary part has a decaying behavior, and in this case, there is more power consumed by $+G$ (loss) than the one provided by $-G$ (gain). A graphical summary of this investigation is presented in Fig. 7(a) where, for each of the three modes associated with a perturbed third order EPD, the propagating, growing, and decaying modes are shown. At the EPD the three modes coalesce to form one degenerate mode with a purely real $k = k_e$.

To better understand the power distribution inside the unit cells, we consider case A: In Fig. 7(b) the power over the three lines of the semi-infinitely long periodic structure is plotted versus normalized z, evaluated exactly at EPD frequency and wave number such that $0 < k_e d < \pi$. The plot was obtained by assuming an input state vector at $z = 0$ is the EPD degenerate eigenvector, $\boldsymbol{\Psi}(z = 0) = \boldsymbol{\Psi}_e$, associated with positive value k_e with $0 < k_e < \pi/d$, and the degenerate state eigenvector has been normalized such that $||\boldsymbol{\Psi}_e|| = \boldsymbol{\Psi}_e^T \boldsymbol{\Psi}_e^* = 2.31\,\mathrm{V}^2$. This eigenvector excites voltages and currents on each of the three TLs. The other degenerate mode with $-k_e$ has a different eigenvector; therefore the one used in this simulation, $\boldsymbol{\Psi}_e$, excites only the three degenerate modes with positive k_e.

In Fig. 7(c), the total power (summation of the powers flowing in the three lines of the circuit, top, middle, and bottom) is plotted versus normalized z. We observe two different jumps in the power in each period that are associated with the power dissipation and contribution of the $+G$ and $-G$ lumped elements to the circuit, respectively. Since this power flow is evaluated exactly at the EPD condition, where the three coalesced wave numbers are purely real, the power entering each unit cell from the left is the same as the one exiting to the right. Therefore, at the EPD the power over $+G$ and $-G$ is balanced, with $P_{-G} = -P_{+G}$. The conservation of the power is also verified in our numerical simulations by directly calculating these two quantities [the plot in Fig. 7(c) is obtained by summing the three powers] where we see that the total power carried by this degenerate mode exiting any unit cell to the right is equal to the power entering it from the left.

We have selected case A for demonstration purposes in Figs. 7(b) and 7(c), but the general concept of the power analysis provided here is analogous with the other two cases featuring third order EPDs. This study provides us with some physical insight into how different modes behave and how the signal and its power are propagating throughout the structure. In the following section, we will provide more investigation of the powers and gain for a finite-length and terminated periodic structure.

III. FINITE-LENGTH STRUCTURE PROPERTIES

As discussed earlier, devices featuring EPDs may exhibit special properties and enhanced characteristics which make them potential candidates for applications. To provide an example application of the regime presented in this paper, we consider a finite-length three-way waveguide constructed by
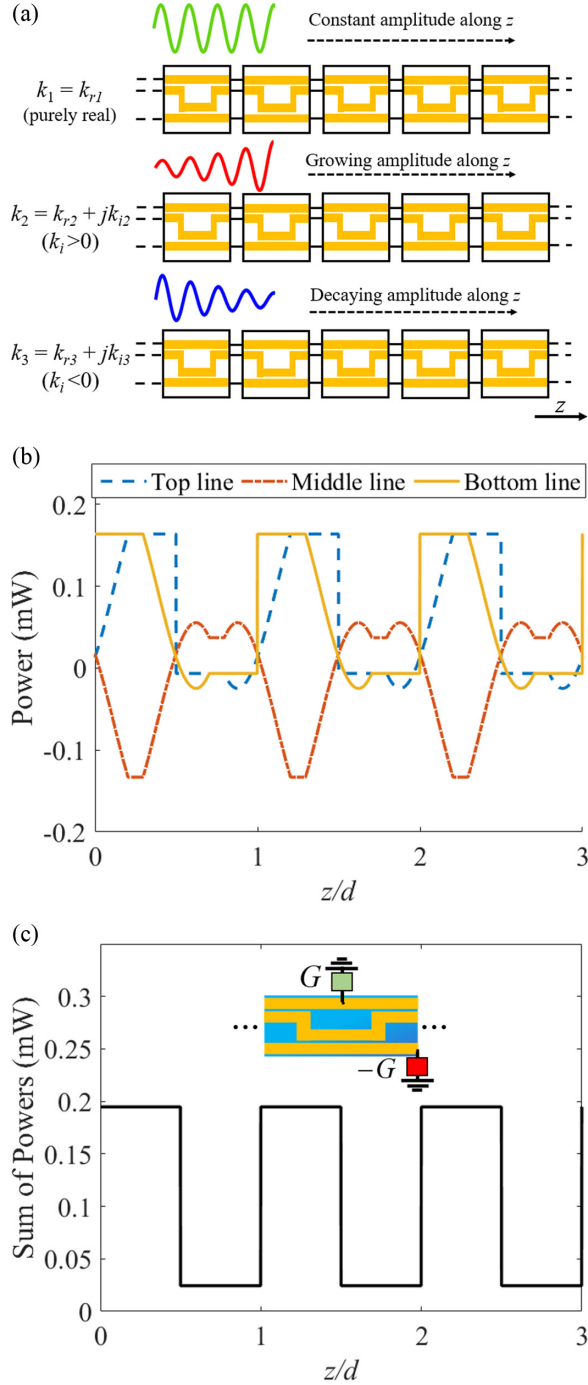
FIG. 7. (a) Graphical representation of how the power propagates along the periodic structure in the $+z$ direction, for three different wave numbers: purely real k_1, and complex wave number with positive imaginary part (k_2), and with negative imaginary part (k_3). (b) Power (in mW) over the three lines of the semi-infinite long periodic structure plotted versus z evaluated exactly at EPD frequency for the design of case A, for the EPD in the region $0 < k_e d < \pi$. This plot exhibits how the power moves over the structure for the specific degenerate eigenmode on each line of the three-way waveguide. (c) Summation of the powers of the three lines shown in part (b), plotted versus z for the semi-infinite periodic circuit. The jumps in the power are associated with the $+G$ and $-G$ contributions.

cascading the proposed $\mathcal{GT}$-symmetric unit cells and adding proper excitation and terminations to make a distributed amplifier, with the $-G$ as distributed gain and with the $+G$ elements as radiative loads (modeling antennas). In this section, we first provide an investigation of the resonance behavior and stability analysis of such finite-length three-way waveguide and then show the amplification at the EPD frequency.

A. Resonance behavior and stability analysis

We consider the three-way waveguide structure of case A in Fig. 2(a), consisting of N cascaded unit cells as depicted in Fig. 8(a). We have omitted the rightmost $-G$ element, as shown, to make the terminated structure symmetric and help to improve stability. We excite the middle line of the three CTLs with terminations of $Z_s = Z_L = 50\,\Omega$. For the terminals of the bottom line, we are assuming $Z_y = 50\Omega$, and for the top line we are assuming short circuit terminations ($Z_x = 0\,\Omega$) as shown in Fig. 8(a). We have selected this loading scenario based on the stability and gain performance of the three-way structure. First, to check the stability and the resonance behavior, we check the S parameters. Based on [70], for two port networks, oscillations are possible when either the input or output port presents a negative resistance, which occurs when $|S_{11}| > 1$ or $|S_{22}| > 1$ in our structure setup, treated as a two-port network (because of symmetry, $S_{11} = S_{22}$). To check stability, we need to evaluate S_{11}. For the design of case A, the results for the S_{11} and S_{21} parameters, assuming $N = 8$ unit cells and lossless structure (besides the lumped elements), are provided in Fig. 8(b) over a wide frequency range. The structure is stable based on the S_{11} response shown in Fig. 8(b). For other configurations or loading scenarios, stability could also be reached by using impedance matching circuits (filters). The S_{21} parameter plotted in Fig. 8(b) versus frequency shows a sharp resonance peak denoted by ω_r associated with the third order EPD frequency of 2 GHz.

B. Gain evaluation

To evaluate the behavior of the proposed distributed amplifier, we consider the power delivered to the loads (Z_L and Z_y) as well as the power delivered to all the N passive elements ($+G$) for different structure lengths. We calculate the load power gain (G_{Loads}) and radiation power gain ($G_{\text{Radiation}}$). In our analysis, the load gain is defined as $G_{\text{Loads}} = P_{\text{Loads-total}}/P_{\text{in}}$ in which $P_{\text{Loads-total}}$ is a summation of the power over Z_L and the two Z_y, and P_{in} is the input power at the second (middle) line input. The radiation gain is defined as $G_{\text{Radiation}} = P_{\text{Radiation-total}}/P_{\text{in}}$, in which $P_{\text{Radiation-total}}$ is the summation of the powers delivered to the $+G$ elements and P_{in} is the input power at the second (middle) line input. All the other parameters are the same as previously discussed for case A.

In Fig. 8(c), the radiation gain and load gain are plotted versus the length of the finite-length structure (N) at the strong-peak resonance frequency nearest to the third order EPD in case A, still assuming absence of losses in the substrate, $\tan(\delta) = 0$, and in the metals. We observe high values of radiation gain, significantly larger than the load gain. These results are based upon the terminations of $Z_y = Z_s = Z_L =$
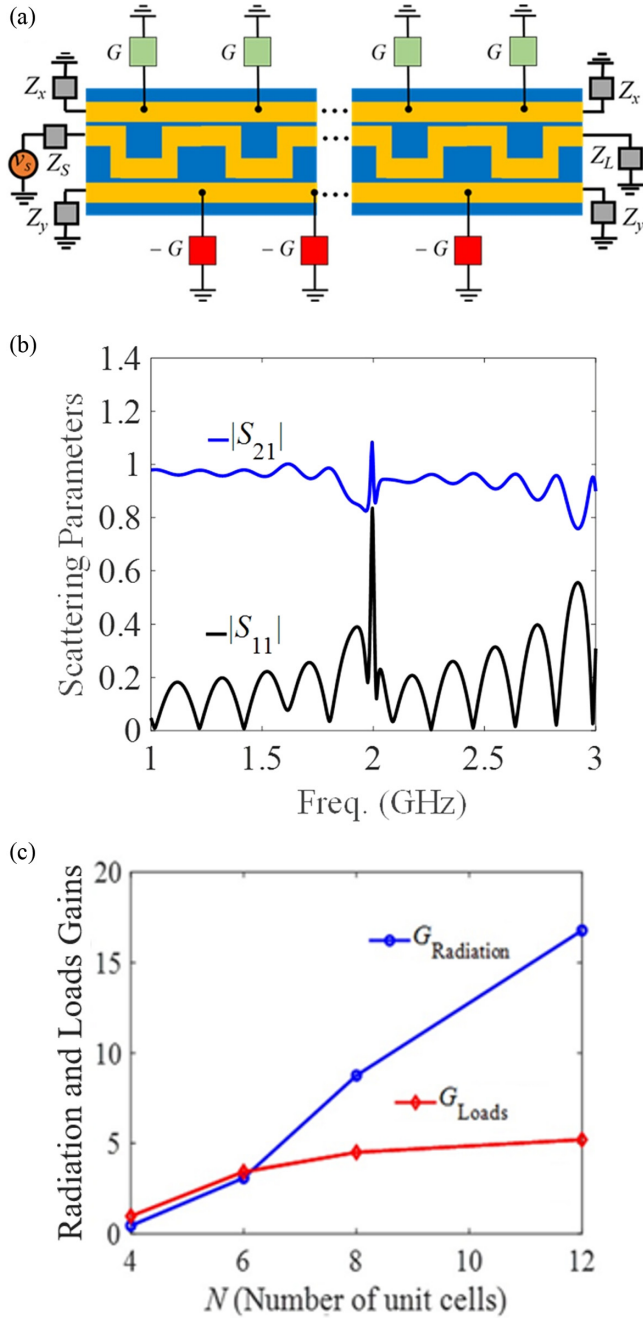
FIG. 8. (a) Finite-length three-way structure with period d made by cascading N unit cells with the total length of $L = Nd$. (b) Plot of $|S_{11}|$ and $|S_{21}|$ for the finite-length structure of case A with $N = 8$ unit cells and substrate with $\tan(\delta) = 0$, around the EPD frequency, $f_e = 2$ GHz, where we observe that $|S_{11}| < 1$ and hence unconditional stability. (c) Radiation gain and loads gain (both in linear scale) versus the length N of the finite structure of case A, evaluated at the strong-peak frequency nearest to the EPD. For all results shown above we have assumed $Z_y = Z_s = Z_L = 50\,\Omega$ for the bottom and middle lines, and two short circuits for the top line ($Z_x = 0\,\Omega$).

$50\,\Omega$ for the bottom and middle lines and two short circuits for the top line ($Z_x = 0\,\Omega$), similar to the previous section. The result of Fig. 8(c) shows that, while being stable, for the case of $N = 8$, we reach a radiation gain of $G_{\text{Radiation}} = 8.8$ for the

passive radiating elements with $+G$, while the load gain has a lower value of $G_L = 4.5$ at the EPD resonance frequency. The radiation gain increases significantly by increasing the radiator's length, which makes the proposed structure a potential scheme for distributed amplifier applications.

IV. CONCLUSION

We have reported the existence of third order EPDs with real-valued wave numbers in three-way waveguides with $\mathcal{GT}$ symmetry. At the EPD, three eigenmodes coalesce at a desired frequency and purely real wave number. Besides having a real-valued wave number in the presence of gain and loss, there is also one branch (solid black, Figs. 1 and 3–5) of the dispersion diagram which has purely real wave numbers.

We have provided two different waveguide configurations and demonstrated how the group velocity of the mode with a purely real wave number can be slightly altered by tuning the physical parameters, which may be beneficial for various applications. A potential scheme using this third order EPD could be in high-gain distributed amplifiers with distributed power extraction. Indeed, the simultaneous presence of distributed gain and losses (modeling radiation conductances) and the same slope sign of the propagating wave number branch (black curves in Figs. 1 and 3–5) at frequencies below and above the EPD frequency, paves the way to a new set of applications of EPDs in high power radiating "apertures." We have briefly discussed such an application and provided the radiation gain analysis for a finite-length array of antennas, where each antenna is represented by a lumped "radiation resistance." The fundamental idea here presented is not limited to the specific design shown in this paper but can be potentially applied to a variety of periodic waveguide structures implemented in different technologies, including EPD lasers with distributed power extraction.

Importantly, the kind of third order EPD studied in this paper is exhibited in the presence of periodic gain and antennas (loss), so arrays of this kind can radiate high power if gain and loss are designed to be large. This is very different from the concept of an SIP (i.e., frozen mode) in a lossless and gainless waveguide, where distributed gain was then introduced as in [58]; in that case, the SIP is increasingly destroyed when higher and higher gain is introduced in each unit cell, whereas the third order EPD in this paper is fully maintained even with large gain elements if properly designed, enabling very high-power applications of EPDs. Examples of a second order EPD in waveguiding structures that exists while high power is continuously extracted along the waveguide are provided in the oscillator concept shown in [51], and in the backward oscillator concept presented in Refs. [50,63,64] leading to high power and high efficiency. Analogously, the third order EPD shown in this paper can be exploited for high-power radiating oscillators, lasers with distributed power extraction, and distributed amplifiers with distributed power extraction.

APPENDIX A: PARAMETERS USED IN SIMULATIONS

In our simulations, we considered a periodic coupled three-way waveguide composed of unit cells, each made of three coupled TLs as in Fig. 2. For all the designs discussed in this paper, the microstrip linewidths are fixed to have $w = 5$ mm (i.e., with 50 Ω characteristic impedance) and $s = 0.5$ mm for the distancing between the lines. The substrate is assumed to have a relative dielectric constant of 2.2, loss tangent of 0 (lossless dielectric), and thickness of $h_s = 1.575$ mm. Metal layers are assumed to be lossless as well.

Case A: The tuned unit-cell parameters that led to an EPD were found to have conductance values of $G = 0.1398$ S (or equivalently $R = 1/G = 7.15$ Ω), serpentine height of $h = 5.35$ mm, and period of $d = 54.15$ mm.

Case B: For this case, the tuned unit-cell parameters have a conductance value of $G = 0.105$ S (or equivalently $R = 1/G = 9.5$ Ω), serpentine height of $h = 6.36$ mm, and period of $d = 46.3$ mm.

Case C: For this case, the tuned parameters have a conductance value of $G = 0.0099$ S (or equivalently $R = 1/G = 100.55$ Ω), serpentine height of $h = 1.07$ mm, and period of $d = 48.08$ mm.

APPENDIX B: TRANSFER MATRIX FORMALISM

1. Transfer matrices for CTLs

In order to construct the transfer matrix and tune the physical unit-cell dimensions to acquire a third order EPD, we have divided the unit cell of the three-way microstrip waveguide into smaller segments as shown in Fig. 9 and modeled each segment to obtain the unit-cell transfer matrix. We built the T-matrix of each segment using TL analytic formulas based on quasistatic models in [71,72].

The transfer matrices of each smaller segment of the unit cell shown in Fig. 1(a) are expressed and calculated in terms of the parameters of the unit cell of the system (length, width, height, separation). Finally, the transfer matrix for the whole unit cell (without the added conductances and gain elements) is obtained by the product of the transfer matrices for each smaller segment of three CTLs inside the unit cell as

$$\underline{\mathbf{T}}_U = \underline{\mathbf{T}}_A \underline{\mathbf{T}}_C \underline{\mathbf{T}}_B \underline{\mathbf{T}}_B \underline{\mathbf{T}}_C \underline{\mathbf{T}}_A. \tag{B1}$$
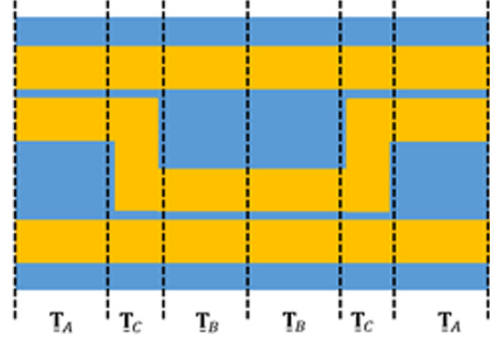

FIG. 9. Unit cell of the three-way periodic microstrip structure over a grounded substrate used to obtain the EPD, divided into smaller segments to construct the corresponding transfer function for each segment in terms. The total transfer matrix of the unit cell is then derived by multiplying the segment transfer matrices.

2. Transfer matrix for lumped conductances

We find the transfer matrices for the added conductance and gain lumped elements in each unit cell. For the first admittance added on the top line with the value of $-G$ (active device) we have

$$\underline{\mathbf{T}}_{+G} = \begin{pmatrix} 1 & 0 & 0 & & & \\ GZ_0 & 1 & 0 & & \mathbf{0}_{3\times3} & \\ 0 & 0 & 1 & & & \\ & \mathbf{0}_{3\times3} & & & \mathbf{I}_{3\times3} & \end{pmatrix}, \tag{B2}$$

where G is the conductance value (assumed positive) of the active gain device. For the second admittance added on the bottom line with the value of G (passive device) we have

$$\underline{\mathbf{T}}_{-G} = \begin{pmatrix} \mathbf{I}_{3\times3} & & & \mathbf{0}_{3\times3} & \\ & & 1 & 0 & 0 \\ \mathbf{0}_{3\times3} & & 0 & 1 & 0 \\ & & 0 & -GZ_0 & 1 \end{pmatrix}. \tag{B3}$$

Therefore, the total transfer matrix for the unit cell of case *A* shown in Fig. 2(a), including the added lumped radiation conductance and gain device, is calculated as

$$\underline{\mathbf{T}}_U = \underline{\mathbf{T}}_{-G} \underline{\mathbf{T}}_A \underline{\mathbf{T}}_C \underline{\mathbf{T}}_B \underline{\mathbf{T}}_{+G} \underline{\mathbf{T}}_B \underline{\mathbf{T}}_C \underline{\mathbf{T}}_A. \tag{B4}$$

The total transfer matrix for the unit cell of case *B* shown in Fig. 2(b), including the added lumped radiation conductance and gain device, is calculated as

$$\underline{\mathbf{T}}_U = \underline{\mathbf{T}}_G \underline{\mathbf{T}}_A \underline{\mathbf{T}}_C \underline{\mathbf{T}}_B \underline{\mathbf{T}}_{-G} \underline{\mathbf{T}}_B \underline{\mathbf{T}}_C \underline{\mathbf{T}}_A. \tag{B5}$$

[1] C. M. Bender and S. Boettcher, Real Spectra in Non-Hermitian Hamiltonians Having $\mathcal{PT}$ Symmetry, Phys. Rev. Lett. **80**, 5243 (1998).

[2] R. El-Ganainy, K. G. Makris, D. N. Christodoulides, and Z. H. Musslimani, Theory of coupled optical $\mathcal{PT}$-symmetric structures, Opt. Lett. **32**, 2632 (2007).

[3] A. Hessel, M. H. Chen, R. C. M. Li, and A. A. Oliner, Propagation in periodically loaded waveguides with higher symmetries, Proc. IEEE **61**, 183 (1973).

[4] A. Figotin and I. Vitebskiy, Electromagnetic unidirectionality in magnetic photonic crystals, Phys. Rev. B **67**, 165210 (2003).

[5] A. Figotin and I. Vitebskiy, Oblique frozen modes in periodic layered media, Phys. Rev. E **68**, 036609 (2003).

[6] A. Figotin and I. Vitebskiy, Gigantic transmission band-edge resonance in periodic stacks of anisotropic layers, Phys. Rev. E **72**, 036619 (2005).

[7] A. Figotin and I. Vitebskiy, Frozen light in photonic crystals with degenerate band edge, Phys. Rev. E **74**, 066613 (2006).

[8] A. Figotin and I. Vitebskiy, Slow-wave resonance in periodic stacks of anisotropic layers, Phys. Rev. A **76**, 053839 (2007).

[9] A. Figotin and I. Vitebskiy, Slow light in photonic crystals, Waves Random Complex Media **16**, 293 (2006).

[10] A. Figotin and I. Vitebskiy, Slow wave phenomena in photonic crystals, Laser Photonics Rev. **5**, 201 (2011).

[11] M. I. Vishik and L. A. Lyusternik, The solution of some perturbation problems for matrices and selfadjoint or non-selfadjoint differential equations I, Russ. Math. Surv. **15**, 1 (1960).

[12] P. Lancaster, On eigenvalues of matrices dependent on a parameter, Numer. Math. **6**, 377 (1964).

[13] T. Kato, *Perturbation Theory for Linear Operators* (Springer-Verlag, New York, 1966).

[14] A. P. Seyranian, Sensitivity analysis of multiple eigenvalues*, Mech. Struct. Mach. **21**, 261 (1993).

[15] W. D. Heiss, M. Müller, and I. Rotter, Collectivity, phase transitions, and exceptional points in open quantum systems, Phys. Rev. E **58**, 2894 (1998).

[16] T. Stehmann, W. D. Heiss, and F. G. Scholtz, Observation of exceptional points in electronic circuits, J. Phys. Math. Gen. **37**, 7813 (2004).

[17] C. E. Rüter, K. G. Makris, R. El-Ganainy, D. N. Christodoulides, M. Segev, and D. Kip, Observation of parity–time symmetry in optics, Nat. Phys. **6**, 192 (2010).

[18] J. Schindler, A. Li, M. C. Zheng, F. M. Ellis, and T. Kottos, Experimental study of active *LRC* circuits with $\mathcal{PT}$ symmetries, Phys. Rev. A **84**, 040101(R) (2011).

[19] S. Bittner, B. Dietz, U. Günther, H. L. Harney, M. Miski-Oglu, A. Richter, and F. Schäfer, $\mathcal{PT}$ Symmetry and Spontaneous Symmetry Breaking in a Microwave Billiard, Phys. Rev. Lett. **108**, 024101 (2012).

[20] H. Ramezani, S. Kalish, I. Vitebskiy, and T. Kottos, Unidirectional Lasing Emerging from Frozen Light in Nonreciprocal Cavities, Phys. Rev. Lett. **112**, 043904 (2014).

[21] H. Hodaei, M.-A. Miri, M. Heinrich, D. N. Christodoulides, and M. Khajavikhan, Parity-time–symmetric microring lasers, Science **346**, 975 (2014).

[22] L. Feng, Z. J. Wong, R.-M. Ma, Y. Wang, and X. Zhang, Single-mode laser by parity-time symmetry breaking, Science **346**, 972 (2014).

[23] Z. Liu, Q. Zhang, X. Liu, Y. Yao, and J.-J. Xiao, Absence of exceptional points in square waveguide arrays with apparently balanced gain and loss, Sci. Rep. **6**, 22711 (2016).

[24] J. Wiersig, Sensors operating at exceptional points: General theory, Phys. Rev. A **93**, 033809 (2016).

[25] A. Ruschhaupt, F. Delgado, and J. G. Muga, Physical realization of $\mathcal{PT}$-symmetric potential scattering in a planar slab waveguide, J. Phys. A: Math. Gen. **38**, L171 (2005).

[26] R. Mittra and S. Laxpati, Propagation in a wave guide with glide reflection symmetry, Can. J. Phys. **43**, 353 (1965).

[27] M. Bagheriasl, O. Quevedo-Teruel, and G. Valerio, Bloch analysis of artificial lines and surfaces exhibiting glide symmetry, IEEE Trans. Microwave Theory Tech. **67**, 2618 (2019).

[28] F. Ghasemifard, M. Norgren, O. Quevedo-Teruel, and G. Valerio, Analyzing glide-symmetric holey metasurfaces using a generalized floquet theorem, IEEE Access **6**, 71743 (2018).

[29] Q. Chen, F. Mesa, X. Yin, and O. Quevedo-Teruel, Accurate characterization and design guidelines of glide-symmetric holey EBG, IEEE Trans. Microwave Theory Tech. **68**, 4984 (2020).

[30] J. Martínez, A. Coves, F. Mesa, and O. Quevedo-Teruel, Passband broadening of sub-wavelength resonator-based glide-symmetric SIW filters, AEU - Int. J. Electron. Commun. **125**, 153362 (2020).

[31] B. A. Mouris, A. Fernandez-Prieto, R. Thobaben, J. Martel, F. Mesa, and O. Quevedo-Teruel, On the increment of the bandwidth of mushroom-type EBG structures with glide symmetry, IEEE Trans. Microwave Theory Tech. **68**, 1365 (2020).

[32] Q. Chen, F. Giusti, G. Valerio, F. Mesa, and O. Quevedo-Teruel, Anisotropic glide-symmetric substrate-integrated-holey metasurface for a compressed ultrawideband Luneburg lens, Appl. Phys. Lett. **118**, 084102 (2021).

[33] O. Quevedo-Teruel, Q. Chen, F. Mesa, N. J. G. Fonseca, and G. Valerio, On the benefits of glide symmetries for microwave devices, IEEE J. Microwaves **1**, 457 (2021).

[34] M. B. Stephanson, K. Sertel, and J. L. Volakis, Frozen modes in coupled microstrip lines printed on ferromagnetic substrates, IEEE Microwave Wireless Compon. Lett. **18**, 305 (2008).

[35] M. A. K. Othman, F. Yazdi, A. Figotin, and F. Capolino, Giant gain enhancement in photonic crystals with a degenerate band edge, Phys. Rev. B **93**, 024301 (2016).

[36] R. Almhmadi and K. Sertel, Frozen-light modes in 3-way coupled silicon ridge waveguides, in *2019 United States National Committee of URSI National Radio Science Meeting (USNC-URSI NRSM)* (2019), pp. 1–2.

[37] B. Paul, N. K. Nahar, and K. Sertel, Frozen mode in coupled silicon ridge waveguides for optical true time delay applications, J. Opt. Soc. Am. B **38**, 1435 (2021).

[38] M. Y. Nada, T. Mealy, and F. Capolino, Frozen mode in three-way periodic microstrip coupled waveguide, IEEE Microwave Wireless Compon. Lett. **31**, 229 (2021).

[39] G. Mumcu, K. Sertel, and J. L. Volakis, Lumped circuit models for degenerate band edge and magnetic photonic crystals, IEEE Microwave Wireless Compon. Lett. **20**, 4 (2010).

[40] J. R. Burr, N. Gutman, C. Martijn de Sterke, I. Vitebskiy, and R. M. Reano, Degenerate band edge resonances in coupled periodic silicon optical waveguides, Opt. Express **21**, 8736 (2013).

[41] M. A. Othman, X. Pan, G. Atmatzakis, C. G. Christodoulou, and F. Capolino, Experimental demonstration of degenerate band edge in metallic periodically loaded circular waveguide, IEEE Trans. Microwave Theory Tech. **65**, 4037 (2017).

[42] T. Mealy and F. Capolino, General conditions to realize exceptional points of degeneracy in two uniform coupled

transmission lines, IEEE Trans. Microwave Theory Tech. **68**, 3342 (2020).

[43] M. Y. Nada, M. A. Othman, and F. Capolino, Theory of coupled resonator optical waveguides exhibiting high-order exceptional points of degeneracy, Phys. Rev. B **96**, 184304 (2017).

[44] X.-Y. Wang, F.-F. Wang, and X.-Y. Hu, Waveguide-induced coalescence of exceptional points, Phys. Rev. A **101**, 053820 (2020).

[45] N. Gutman, C. Martijn de Sterke, A. A. Sukhorukov, and L. C. Botten, Slow and frozen light in optical waveguides with multiple gratings: Degenerate band edges and stationary inflection points, Phys. Rev. A **85**, 033804 (2012).

[46] H. Li, I. Vitebskiy, and T. Kottos, Frozen mode regime in finite periodic structures, Phys. Rev. B **96**, 180301(R) (2017).

[47] A. F. Abdelshafy, M. A. K. Othman, D. Oshmarin, A. T. Almutawa, and F. Capolino, Exceptional points of degeneracy in periodic coupled waveguides and the interplay of gain and radiation loss: Theoretical and experimental demonstration, IEEE Trans. Antennas Propag. **67**, 6909 (2019).

[48] A. A. Chabanov, Strongly resonant transmission of electromagnetic radiation in periodic anisotropic layered media, Phys. Rev. A **77**, 033811 (2008).

[49] G. Castaldi, S. Savoia, V. Galdi, A. Alù, and N. Engheta, $\mathcal{PT}$ Metamaterials via Complex-Coordinate Transformation Optics, Phys. Rev. Lett. **110**, 173901 (2013).

[50] T. Mealy, A. F. Abdelshafy, and F. Capolino, Exceptional Point of Degeneracy in a Backward-Wave Oscillator with Distributed Power Extraction, Phys. Rev. Appl. **14**, 014078 (2020).

[51] A. F. Abdelshafy, T. Mealy, E. Hafezi, A. Nikzamir, and F. Capolino, Exceptional degeneracy in a waveguide periodically loaded with discrete gain and radiation loss elements, Appl. Phys. Lett. **118**, 224102 (2021).

[52] S. Jiang, X. Chang, W. Li, P. Han, Y. Zhou, H. Zhang, A. Huang, and Z. Xiao, On-chip high sensitivity rotation sensing based on higher-order exceptional points, J. Opt. Soc. Am. B **36**, 2618 (2019).

[53] Q. Wang, J. Wang, H. Z. Shen, S. C. Hou, and X. X. Yi, Exceptional points and dynamics of a non-Hermitian two-level system without $\mathcal{PT}$ symmetry, EPL **131**, 34001 (2020).

[54] I. Mandal and E. J. Bergholtz, Symmetry and Higher-Order Exceptional Points, Phys. Rev. Lett. **127**, 186601 (2021).

[55] H. Qi, X. Hu, X. Wang, and Q. Gong, Encircling an exceptional point in a multiwaveguide anti–parity-time-symmetry system, Phys. Rev. A **103**, 063520 (2021).

[56] L. Xiao, T. Deng, K. Wang, Z. Wang, W. Yi, and P. Xue, Observation of Non-Bloch Parity-Time Symmetry and Exceptional Points, Phys. Rev. Lett. **126**, 230402 (2021).

[57] L. Ding, K. Shi, Q. Zhang, D. Shen, X. Zhang, and W. Zhang, Experimental Determination of $\mathcal{PT}$-Symmetric Exceptional Points in a Single Trapped Ion, Phys. Rev. Lett. **126**, 083604 (2021).

[58] F. Yazdi, M. A. K. Othman, M. Veysi, A. Figotin, and F. Capolino, A new amplification regime for traveling wave tubes with third-order modal degeneracy, IEEE Trans. Plasma Sci. **46**, 43 (2018).

[59] D. Oshmarin, F. Yazdi, M. A. Othman, J. Sloan, M. Radfar, M. M. Green, and F. Capolino, New oscillator concept based on band edge degeneracy in lumped double-ladder circuits, IET Circuits Devices Syst. **13**, 950 (2019).

[60] A. F. Abdelshafy, D. Oshmarin, M. A. K. Othman, M. M. Green, and F. Capolino, Distributed degenerate band edge oscillator, IEEE Trans. Antennas Propag. **69**, 1821 (2021).

[61] A. M. Zuboraj, B. K. Sertel, and C. J. L. Volakis, Propagation of Degenerate Band-Edge Modes Using Dual Nonidentical Coupled Transmission Lines, Phys. Rev. Appl. **7**, 064030 (2017).

[62] D. Oshmarin, A. F. Abdelshafy, A. Nikzamir, M. M. Green, and F. Capolino, Experimental demonstration of a new oscillator concept based on degenerate band edge in microstrip circuit, arXiv:2109.07002.

[63] T. Mealy, A. F. Abdelshafy, and F. Capolino, High-Power X-Band Relativistic Backward-Wave Oscillator with Exceptional Synchronous Regime Operating at an Exceptional Point, Phys. Rev. Appl. **15**, 064021 (2021).

[64] T. Mealy, A. F. Abdelshafy, and F. Capolino, High-power backward-wave oscillator using folded waveguide with distributed power extraction operating at an exceptional point, IEEE Trans. Electron Devices **68**, 3588 (2021).

[65] M. Lawrence, N. Xu, X. Zhang, L. Cong, J. Han, W. Zhang, and S. Zhang, Manifestation of $\mathcal{PT}$ Symmetry Breaking in Polarization Space with Terahertz Metasurfaces, Phys. Rev. Lett. **113**, 093901 (2014).

[66] N. M. Garcia, I. de Erausquin, C. Edmiston, and V. Gruev, Surface normal reconstruction using circularly polarized light, Opt. Express **23**, 14391 (2015).

[67] S. Buddhiraju, A. Song, G. T. Papadakis, and S. Fan, Nonreciprocal Metamaterial Obeying Time-Reversal Symmetry, Phys. Rev. Lett. **124**, 257403 (2020).

[68] T. G. Mackay and A. Lakhtakia, Polarization-state-dependent attenuation and amplification in a columnar thin film, J. Opt. **19**, 12LT01 (2017).

[69] A. Cerjan and S. Fan, Achieving Arbitrary Control over Pairs of Polarization States Using Complex Birefringent Metamaterials, Phys. Rev. Lett. **118**, 253902 (2017).

[70] G. Gonzalez, *Microwave Transistor Amplifiers Analysis and Design* (Prentice-Hall, Inc., Hoboken, NJ, 1996).

[71] E. Hammerstad and O. Jensen, Accurate models for microstrip computer-aided design, in *1980 IEEE MTT-S International Microwave Symposium Digest* (1980), pp. 407–409.

[72] M. Kirschning and R. H. Jansen, Accurate wide-range design equations for the frequency-dependent characteristics of parallel coupled microstrip lines (Corrections), IEEE Trans. Microwave Theory Tech. **33**, 288 (1985).